Chapter 4

Synthesis and Characterization of $Pd_3Cu_{0.5}Ni_{0.5}$/C and Pd_2CuCo/C Nanoparticles and Their Oxygen Reduction Reaction Activity

Outline

The development of highly efficient electrode materials is very crucial for enhancing fuel cell efficiency as well as to ensure penetrability in the global energy market. Until now, electrocatalysts (ECs) based on Pt and its alloys are the most active catalyst due to their high efficiency for enhancing the sluggish cathodic ORR [1,2]. Unfortunately, low abundance of Pt and poor durability restrict the possible large-scale commercialization of fuel cells. To overcome the above-mentioned shortcomings, Pd based nanocatalyst is an attractive alternative due to its high abundance in nature, the similar lattice constant with Pt and comparable to or even better activity than that of Pt [3-5], for catalysing ORR. To further increase the catalytic efficiency of Pd-based materials for the fuel cell reactions, the Pd lattice is incorporated with transition metals, which can modulate the lattice strain of Pd atoms and alter the d-band centre of the Pd that controls oxygen binding activity [6,7]. Additionally, the cost of catalyst is also reduced by the incorporation of non-precious metals. The shape of NPs has a significant effect on tailoring their overall catalytic performance [8]. To increase the efficiency of ECs, many efforts have focused on fabrication of EC with controllable shape [9] like 3-D nanosheet [10], nano thorn [11] hollow echinus [12] concave decahedra [13], nanobranches [14], branched alloy networks [15], hollow sphere [16] octahedron[17], nanosphere [18] and 5-fold twinned [19] etc.

In this chapter 4, we have discussed about the synthesis, characterization and activity of $Pd_3Cu_{0.5}Ni_{0.5}$/C and Pd_2CuCo/C NPs for ORR . The chapter is divided into two sections:

Section 4A: Synthesis and Characterization of $Pd_3Cu_{0.5}Ni_{0.5}$/C Nanoparticles and their Oxygen Reduction Reaction Activity.

Section 4B: Tuning the Electrocatalytic Activity of Pd_2CuCo/C Nanoparticles towards Fuel Cell Oxygen Reduction Reaction.

Section 4A: Synthesis and Characterization of Pd$_3$Cu$_{0.5}$Ni$_{0.5}$/C Nanoparticles and their Oxygen Reduction Reaction Activity

Section 4A of the chapter 4 describes the synthesis and characterization of Pd$_3$Cu$_{0.5}$Ni$_{0.5}$/C NPs by simple one step solvothermal method using NH$_2$NH$_2$.6H$_2$O as reducing agent. To evaluate the electrocatalytic ORR properties of Pd$_3$Cu$_{0.5}$Ni$_{0.5}$/C, the CV, LSV and CA tests were performed.

4A.1. Results and Discussion

4A.1.1. Characterization of Pd$_3$Cu$_{0.5}$Ni$_{0.5}$/C NPs

The compositions of as prepared NPs are determined by ICP-OES analyses. The Pd, Cu and Ni atomic ratio are *ca.* 72.62%, 12.2% and 10.30%. The loading of the metal obtained by TGA analysis is ~20% in the case of the Pd$_3$Cu$_{0.5}$Ni$_{0.5}$/C (Figure 4A.1). It shows a speedy weight loss of the NPs at about ~350 °C which is due to the oxidation of carbon to carbon dioxide in the adequate air environment. The residue obtained after burning of all the carbon compounds gives information about the loading of the total metal content. The powder XRD patterns of Pd$_3$Cu$_{0.5}$Ni$_{0.5}$/C and Pd/C (Figure 4A.2a) show mainly characteristic peaks of fcc crystalline Pd structure. The diffraction peaks centred at ~40°, ~47°, and ~68° correspond to the (111), (200), and (220) reflections, respectively.
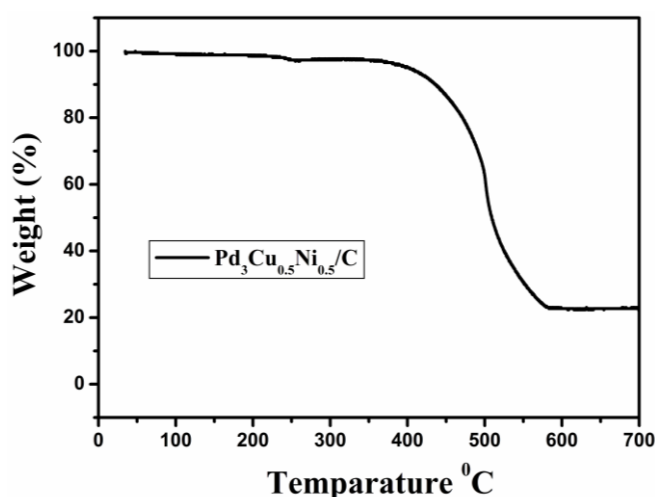

Figure 4A.1: TGA plots of Pd$_3$Cu$_{0.5}$Ni$_{0.5}$/C NPs at air atmosphere.

These peaks are slightly shifted to higher angles relative to the pure Pd (JCPDS no. 87-0641) indicating the formation of an alloyed NPs [20]. A broad peak observed at around ~25° is ascribed to the (002) reflection of a hexagonal structure in Vulcan XC-72 R carbon. The Figure 4A.2b shows the N_2 adsorption-desorption isotherm of $Pd_3Cu_{0.5}Ni_{0.5}$/C which exhibits a high BET specific surface area of 58.8 m²/g and a Pore Diameter 15.7 Å.
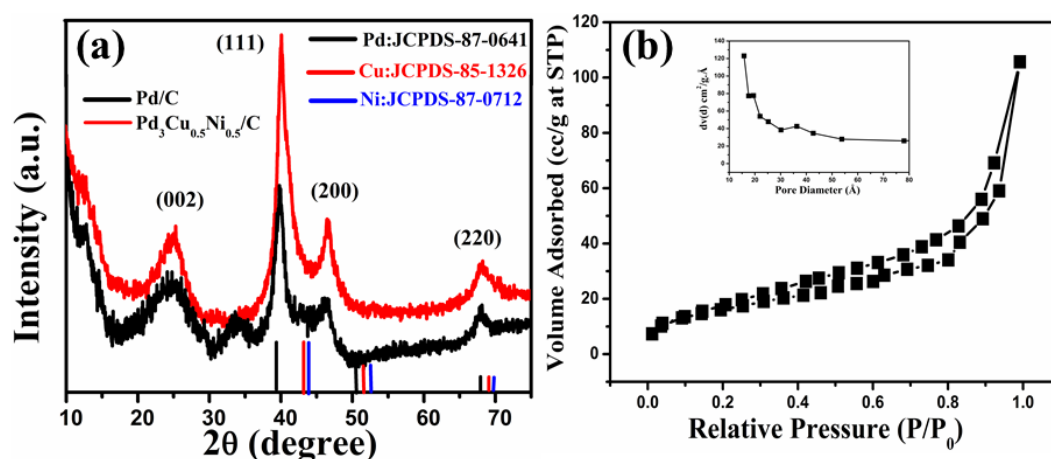

Figure 4A.2: (a) XRD pattern of $Pd_3Cu_{0.5}Ni_{0.5}$/C and Pd/C NPs. (b) N_2 adsorption-desorption isotherm of $Pd_3Cu_{0.5}Ni_{0.5}$/C, inset of (b) shows the pore size distribution.

The shape and microstructure of $Pd_3Cu_{0.5}Ni_{0.5}$/C NPs are further studied by TEM and HR-TEM and presented in Figure 4A.3. From the TEM images (Figure 4A.3a,b) it could be observed that many nearly-spherical $Pd_3Cu_{0.5}Ni_{0.5}$ NPs are highly dispersed on the larger particles of Vulcan XC-72 R carbon. Figure 4A.3c,d reveals that the $Pd_3Cu_{0.5}Ni_{0.5}$ crystallizes as nanowire like structures. The comprehensible *d*-spacings ~0.22 nm (Figure 4A.3f) can be observed in the lattice fringes of a $Pd_3Cu_{0.5}Ni_{0.5}$/C NPs, close to the fcc Pd (111) facets.
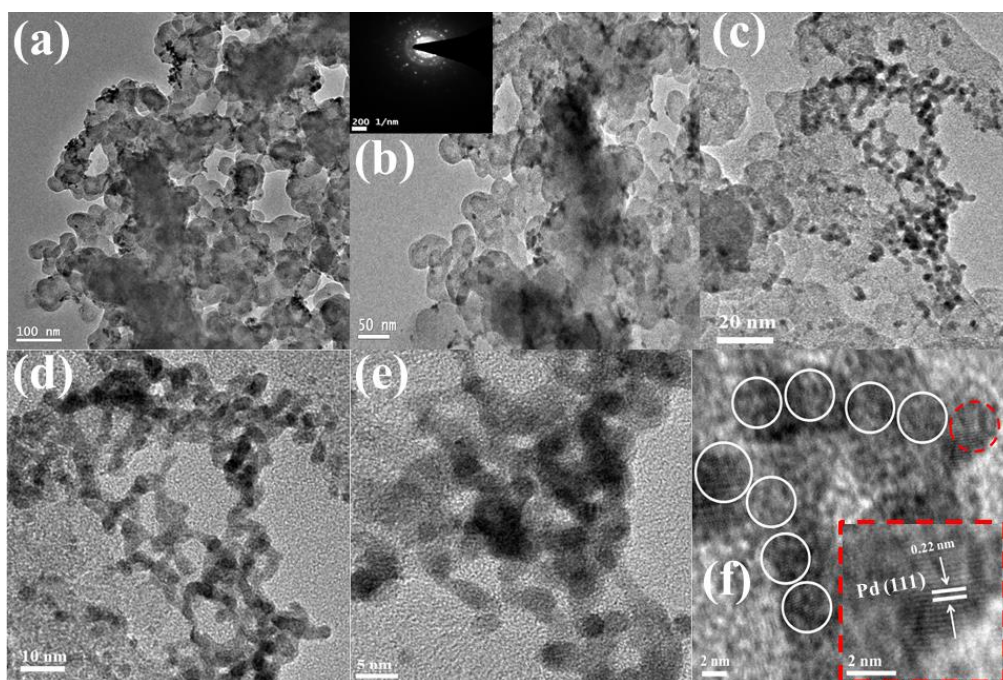
Figure 4A.3: TEM (a-d) and HRTEM (e,f) images of $Pd_3Cu_{0.5}Ni_{0.5}/C$.

XPS is extensively performed to elucidate the chemical composition of NPs. Figure 4A.4a-d illustrates the XP spectra of C 1s, Pd 3d, Cu 2p and Ni 2p regions of $Pd_3Cu_{0.5}Ni_{0.5}/C$. The C 1s core-level XP spectrum (Figure 4A.4a) of $Pd_3Cu_{0.5}$ $Ni_{0.5}/C$ is slightly asymmetric and hence, can be deconvoluted into three different peaks viz., a prominent peak at 284.6 eV along with two small peaks at 285.9 and 289.8 eV, consistent to form −C=C−, −C−O−, and O=C−O− bonds, respectively [21,22]. The Pd 3d XP spectrum as presented in Figure 4A.4b displays a doublet signal with binding energies of 335.5 and 340.8 eV for Pd $3d_{5/2}$ and Pd $3d_{3/2}$, respectively, corresponding to the Pd. Additionally, small doublets observed around 337.2 and 342.7 eV could be indexed to the Pd $3d_{5/2}$ and Pd $3d_{3/2}$ peaks of PdO [23]. The peaks observed at 932.0 and 952.0 eV from the Cu $2p_{3/2}$ and Cu $2p_{1/2}$ spin−orbit doublets, respectively, correspond to a metallic copper (Figure 4A.4c), which is consistent with Cu NPs [24]. Figure 4A.4d shows the Ni 2p core-level spectrum for the NP. Two prominent peaks at 856.3 and 874.0 eV corresponds to the Ni $2p_{3/2}$ and Ni $2p_{1/2}$ core-level energies of nickel oxide.
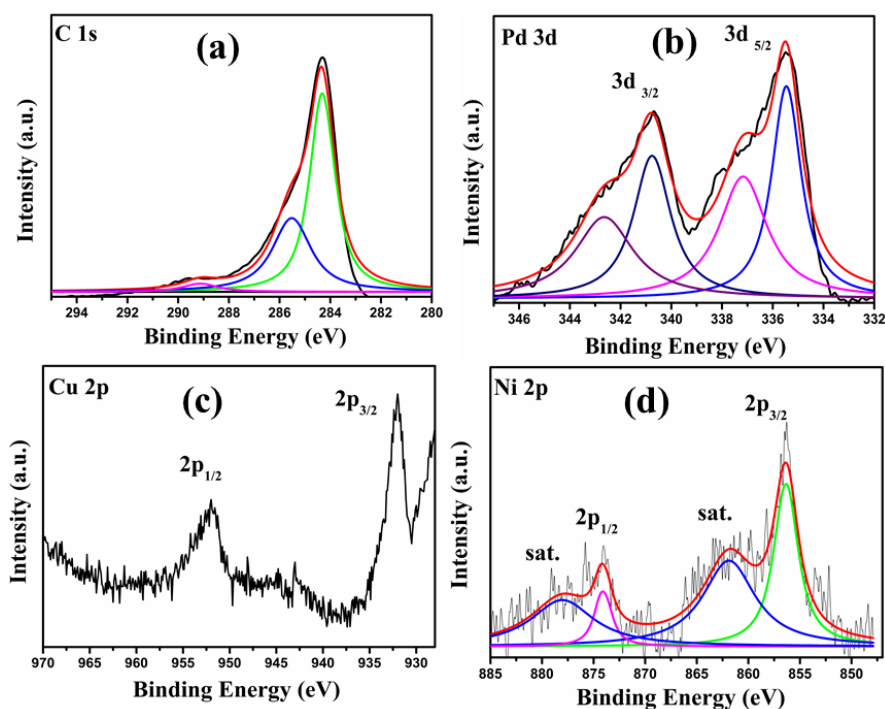
Figure 4A.4: XP spectrum of C 1s (a), Pd 3d (b), Cu 2p (c) and Ni 2p (d) of $Pd_3Cu_{0.5}Ni_{0.5}$/C.

4A.1.2. Electrocatalytic Activity

The electrocatalytic behaviour of $Pd_3Cu_{0.5}Ni_{0.5}$/C NPs modified GCE is measured in N_2- and O_2-saturated 0.1 M KOH, as shown in Figure 4A.5. As presented in the cyclic voltammogram (CV) in Figure 4A.5a, a strong and well-defined reduction peak is observed in O_2-saturated 0.1 M KOH solution whereas no such feature is observed in N_2-saturated electrolyte. This signifies that $Pd_3Cu_{0.5}Ni_{0.5}$/C NP shows good ORR activity. To determine the kinetics of ORR, RDE measurement is performed in O_2-saturated 0.1 M KOH solution at a rotating rate of 400, 900, 1600, 2500 and 3600 rpm as shown in Figure 4A.5b. Based on the ORR polarization curves, "n" transferred during ORR can be evaluated using the K−L equation (see chapter 3) [25].
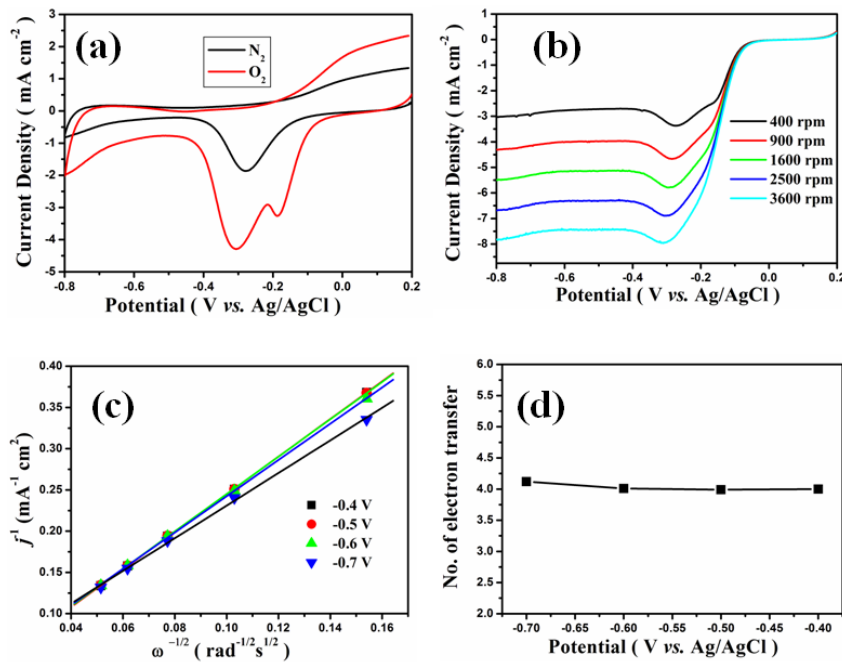
Figure 4A.5: (a) CV plots of $Pd_3Cu_{0.5}Ni_{0.5}$/C, N_2- and O_2-saturated 0.1 M KOH solution with a scan rate of 50 mV s^{-1}, (b) Rotating rate-dependent ORR polarization curves for respective NPs with the scan rate of 10 mV s^{-1}, (c) K-L plots of j^{-1} vs. $\omega^{-1/2}$ for $Pd_3Cu_{0.5}Ni_{0.5}$/C at different potentials obtained from (b), and (d) The plot of the number of transferred electrons *vs.* potential for $Pd_3Cu_{0.5}Ni_{0.5}$/C.

The K−L plots obtained on the basis of the corresponding ORR polarization curves for $Pd_3Cu_{0.5}Ni_{0.5}$/C NP at a potential of −0.40, −0.50, −0.60, and −0.70 V show good linearity (Figure 4A.5c) thereby implying first-order kinetics. Figure 4A.5d gives the corresponding plot of 'n' vs. potential (V). It can be seen that the 'n' values from −0.40 to −0.70 V are ~4.0, suggesting that the ORR mechanism on $Pd_3Cu_{0.5}Ni_{0.5}$/C NPs follows the direct "4e−" pathway ($O_2 + 2H_2O + 4e^- \rightarrow 4OH^-$). To elucidate the electrocatalytic behaviour of the NPs, the ECSA are calculated using CV curves in N_2-saturated 0.1 M KOH (Figure 4A.6). The peaks in the potential range −0.5 to 0 V originates from the palladium oxide reduction [26]. The calculated ECSA of $Pd_3Cu_{0.5}Ni_{0.5}$/C (68.59 m^{2}g^{-1}) is higher than standard Pt/C (8.7 m^{2}g^{-1}), and standard Pd/C (1.42 m^{2}g^{-1}). The higher ECSA values of ternary NPs can be attributed to the synergistic effect.
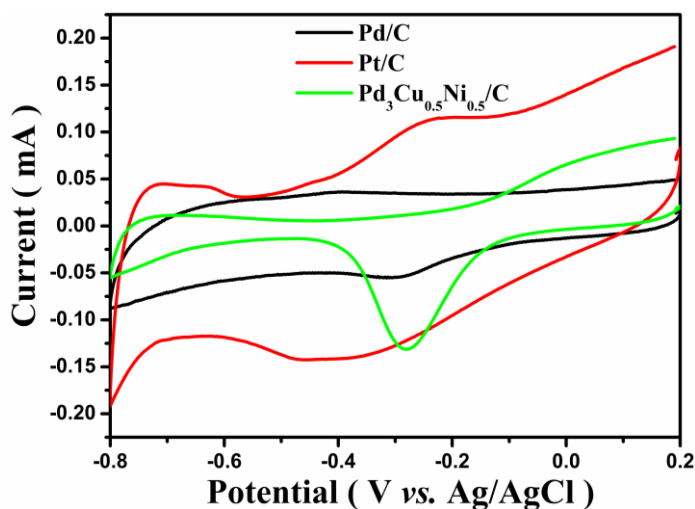
Figure 4A.6: CV plots of various NPs in the N_2-saturated 0.1 M KOH solution with a scan rate of 50 mV s^{-1}.
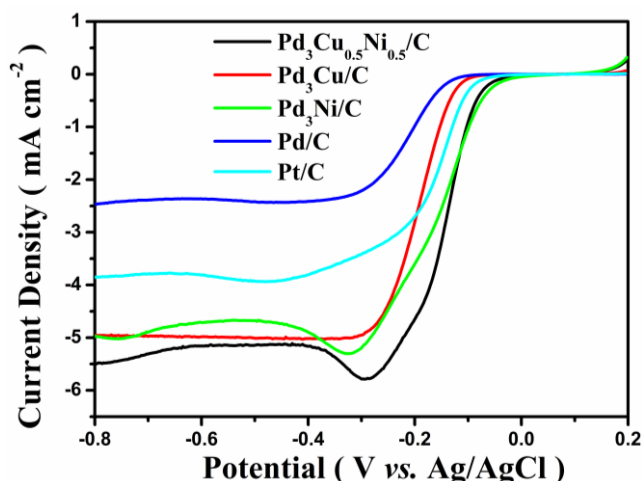

Figure 4A.7: Comparison of rotating rate-dependent ORR polarization curves for different NPs at 1600 rpm.

The onset potential (E_{onset} = −0.044 V) and half-wave potential ($E_{1/2}$ = −0.144 V) of $Pd_3Cu_{0.5}Ni_{0.5}$/C NP are found to be more positive than those of standard Pd/C (E_{onset} = −0.103 V, $E_{1/2}$ = −0.212 V), Pt/C (E_{onset} = −0.069 V, $E_{1/2}$ = −0.154 V), Pd_3Cu/C (E_{onset} = −0.08 V, $E_{1/2}$ = −0.190 V), Pd_3Ni/C (E_{onset} = −0.036 V, $E_{1/2}$ = −0.148 V), under identical conditions, suggesting superior ORR activity of the ternary $Pd_3Cu_{0.5}Ni_{0.5}$/C NP. The overall ORR behaviour follows the order: $Pd_3Cu_{0.5}Ni_{0.5}$/C >

$Pd_3Ni/C > Pd_3Cu/C > Pt/C > Pd/C$. Moreover, the apparent current density values follow the same order.

The Tafel plots derived from the ORR polarization curves for all NPs are presented in Figure 4A.8. The Tafel slope calculated for $Pd_3Cu_{0.5}Ni_{0.5}/C$ is 66.27 mV dec^{-1}. These slopes are smaller than those of Pt/C (84 mV dec^{-1}) and Pd/C (92.38 mV dec^{-1}) respectively. This signifies that $Pd_3Cu_{0.5}Ni_{0.5}/C$ has higher efficiency towards ORR as compared to that of the other catalyst systems studied.
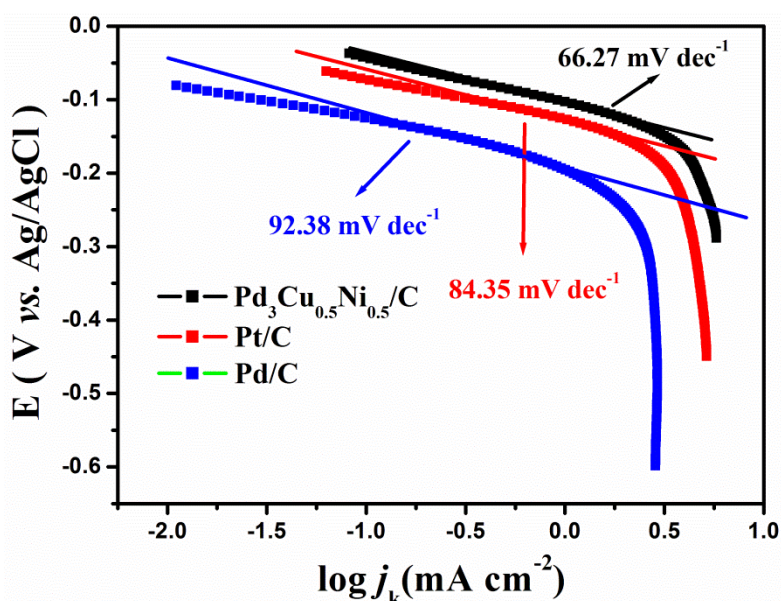

Figure 4A.8: Tafel plots of the $Pd_3Cu_{0.5}Ni_{0.5}/C$, Pd_3Cu/C and Pd_3Ni/C NPs.

The MA and SA are the two important parameters for better assessment of the ORR activity. The MA and SA of various NPs under different potential at 1600 rpm are presented in Figure. 4A.9. The MA and SA of $Pd_3Cu_{0.5}Ni_{0.5}/C$ at −0.4 V (3561 mA mg^{-1} and 75 mA cm^{-2}) are much higher than Pt/C (1900 mA mg^{-1} and 51.89 mA cm^{-2}) and Pd/C (1200 mA mg^{-1} and 33.06 mA cm^{-2}) under the identical experimental conditions. The MA and SA values of $Pd_3Cu_{0.5}Ni_{0.5}/C$ are also larger than those of the Pd_3Cu/C (3316.4 mA mg^{-1} and 69.9 mA cm^{-2}) > Pd_3Ni/C (3196.6 mA mg^{-1} and 67.1 mA cm^{-2}). These experimental findings showed that $Pd_3Cu_{0.5}Ni_{0.5}/C$ NPs as an auspicious ORR EC.
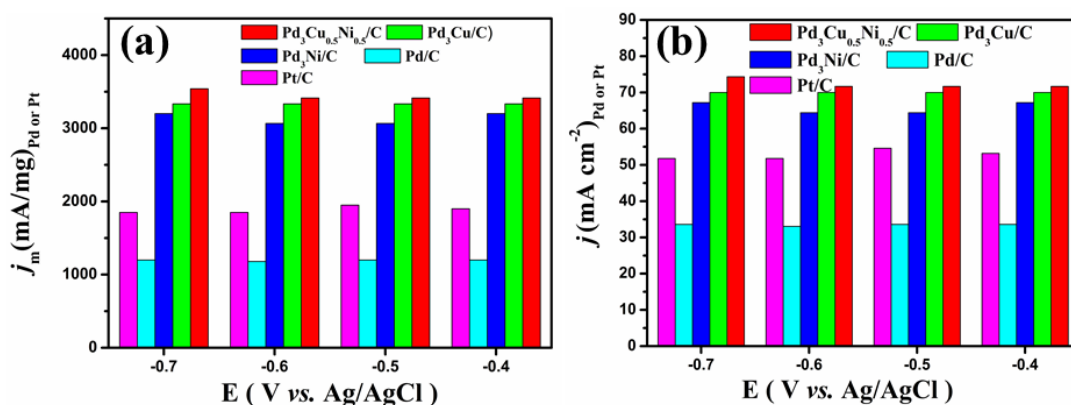
Figure 4A.9: (a) Mass activities and (b) Specific activity of EC under different potential at 1600 rpm. (These values are calculated as per the loading mass of the EC).
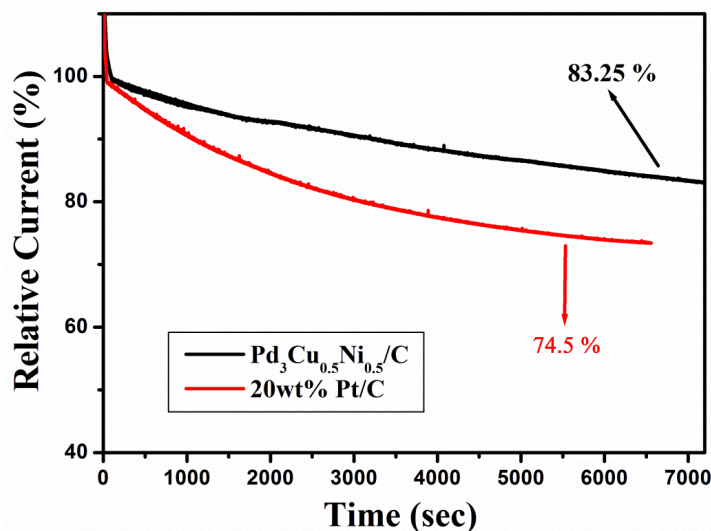
Figure 4A.10: CA curves of different catalysts, recorded at −0.3 V in a O_2-saturated 0.1 M KOH solution with a rotation rate of 1600 rpm towards ORR.

The high durability of the ECs towards ORR is also an important parameter for energy conversion devices. Thus to check the durability, CA test was performed in O_2-saturated 0.1 M KOH at −0.3V (*vs.* Ag/AgCl) with a rotation speed of 1600 rpm. It can be observed from Figure. 4A.10 that the initial activity decay for Pt/C and $Pd_3Cu_{0.5}Ni_{0.5}$/C NP are ~25.5% and ~16.75%, respectively after 7200 sec of testing,

under identical experimental conditions. This demonstrates the excellent stability of the $Pd_3Cu_{0.5}Ni_{0.5}/C$ NPs.

4A.2. Conclusions

An effective and durable ORR EC, $Pd_3Cu_{0.5}Ni_{0.5}/C$ has been synthesized successfully. The unique nanowire structure of the nanoalloy offers stable electronic coupling between the carbon matrix and $Pd_3Cu_{0.5}Ni_{0.5}/C$. The trimetallic $Pd_3Cu_{0.5}Ni_{0.5}$ shows the best electrocatalytic activity among the bimetallic Pd_3Cu/C, Pd_3Ni/C commercial Pd/C and Pt/C ECs in terms of MA and SA as well as current density.

Section 4B: Tuning the Electrocatalytic Activity of Pd₂CuCo/C towards Fuel Cell Oxygen Reduction Reaction

In this section, Pd$_2$CuCo/C nano flowers (PCCC NFs) like NPs were synthesized via facile one step solvothermal process using hydrazine hydrate as a reducing agent and studied their catalytic activity for the electrocatalytic ORR in both acidic and basic media.

4B.1 Results and Discussion

4B.1.1 Structural Characterization

The atomic ratio of the as-synthesized sample was determined by ICP-OES and EDS analysis (Figure 4B.1). The result shows that the atomic ratio of the Pd:Cu:Co in the PCCC NFs was 2:1:1.

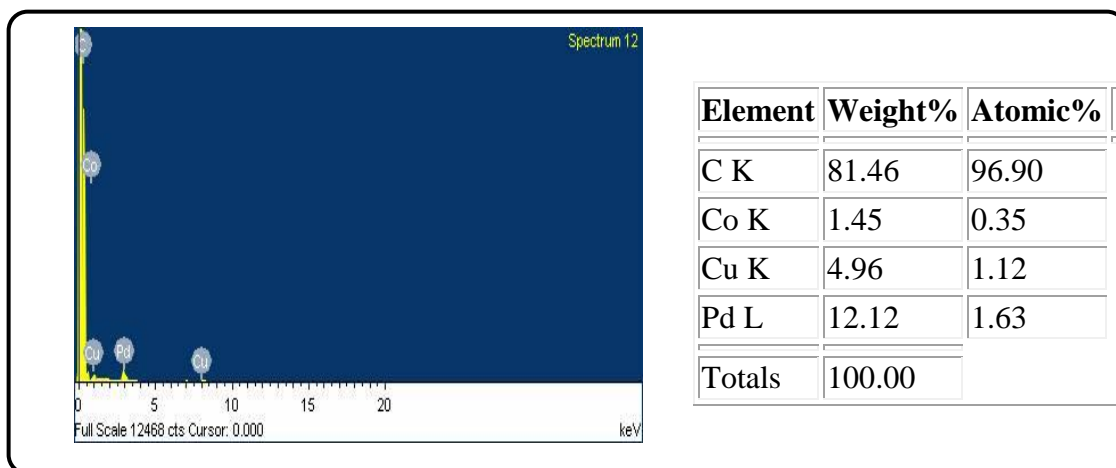| Element	Weight%	Atomic%
C K	81.46	96.90
Co K	1.45	0.35
Cu K	4.96	1.12
Pd L	12.12	1.63
Totals	100.00	

Figure 4B.1: EDS spectrum of the Pd$_2$CuCo/C NFs.

The total metal loading on carbon matrix was also analysed by TGA under air atmosphere, after burning of all carbon at 450 °C, leaving a residue content of ~23% corresponding to the amount of metal accommodated on the carbon matrix as presented in (Figure 4B.2).
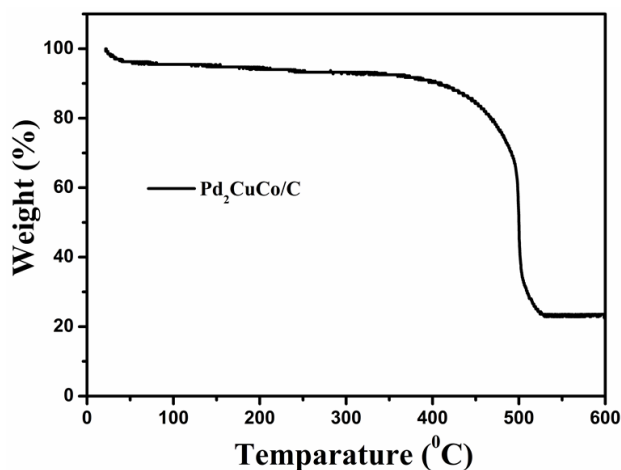
Figure 4B.2: TGA profile of Pd$_2$CuCo/C NFs in air atmosphere.

Figure 4B.3: XRD patterns (a), XP spectrum of Pd 3d (b), Cu 2p (c) and Co 2p (d) of Pd$_2$CuCo/C NFs.

The XRD patterns of PCCC NFs and Pd/C (Figure. 4B.3a) showed pure fcc phase of crystalline Pd (JCPDS 87-0641). The diffraction peaks centred at ~40, ~47, and ~68° correspond to the (111), (200), and (220) reflections, respectively and a broad peak at ~25° corresponds to the (002) reflection of hexagonal structure in

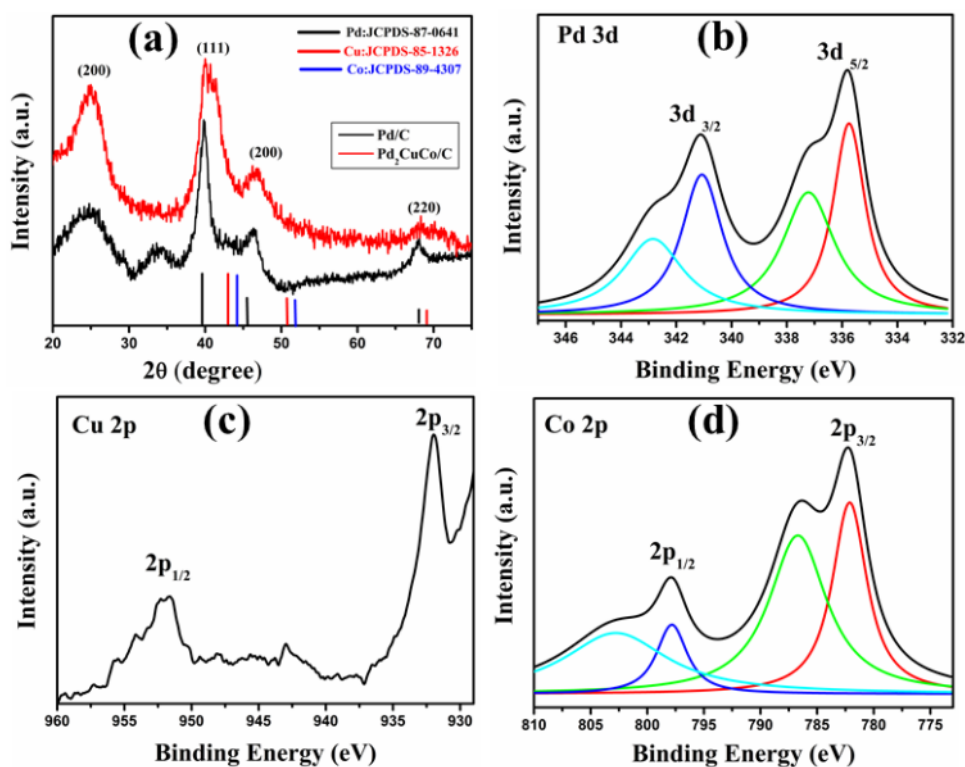Vulcan carbon (XC-72 R). Relative to Pd/C the diffraction peaks of PCCC NFs are slightly shifted to higher angles. The shift of diffraction peaks suggests the formation of alloyed NPs [20]. The calculated d_{111} for PCCC NFs (0.2203 nm) is smaller than Pd/C (0.2264 nm) and higher than Co (JCPDS 89-4307, d_{111} = 0.2046 nm), and Cu (JCPDS 85-1326, d_{111} = 0.2087 nm). It is due to the incorporation of smaller elements suggesting the formation of PdCuCo trimetallic alloys. The observed smaller d_{111} of PCCC NFs relative to Pd/C strengthens the assumption of a more effective lattice strain. Additionally, presence of highly intense (111) peak relative to (200) and (220) peaks infer the preferential exposure of (111) plane [17,27].

To obtain the surface composition XPS was performed. The core-level Pd 3d spectrum can be deconvoluted into two components with binding energies of 335.8 and 337.2 eV for Pd $3d_{5/2}$, which are attributed to Pd^0 and Pd^{2+}, respectively, as shown in Figure. 4B.3b. The peaks at 341.2 and 342.9 eV are assigned to Pd $3d_{3/2}$ [12]. Figure. 4B.3c shows the signature peaks corresponding to Cu $2p_{3/2}$ and Cu $2p_{1/2}$ at 932 and 951.6 eV, respectively for Cu^0. The core-level Co 2p XP spectrum with two major peaks (Co $2p_{3/2}$ = 778.2 and $2p_{1/2}$ = 797.8 eV) which signifies the existence of metallic Co [28]. The two satellite peaks at ~786.8 and 803.0 eV are characteristic of oxidized Co-species [28], as presented in Figure. 4B.3d. A comparison of Pd 3d XP spectra of PCCC NFs and Pd/C is presented in Figure 4B.4. It shows that a positive shift of ~0.50 eV for PCCC NFs relative to Pd/C due to the strong charge transfer between Pd with Cu and Co. This signifies the formation of alloy and also validates the incorporation of Cu and Co into Pd lattice modifying the electronic structure of NFs.
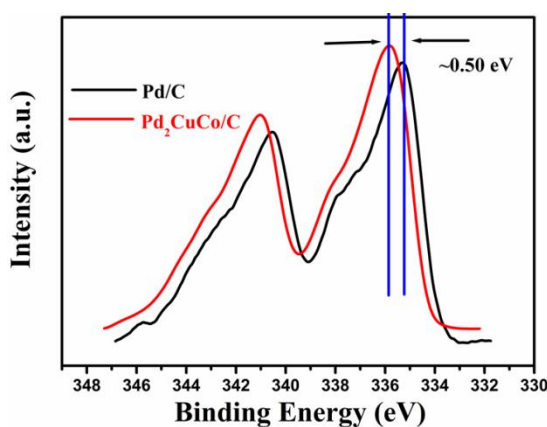

Figure 4B.4: Correlation of binding energy change of Pd 3d in Pd_2CuCo/C NFs and Pd/C.

The TEM images in Figure 4B.5 reveals that the PCCC crystallizes as flower-like structures and the size ranges within 14-18 nm with an average particle cross-sectional diameter of ~16 nm. The HRTEM image in Figure 4B.5d further provides more information on the PCCC NFs. The calculated d-spacing (0.22 nm) from the lattice fringes of PCCC NFs suggests the presence of (111) crystal plane exclusively [29]. This strongly corroborates with XRD results. Furthermore, the NFs exhibit various crystal defects on their surfaces, such as, twin boundary and vacancy defect, which could serve as highly active sites, successfully enhancing the electrocatalytic activity [30].
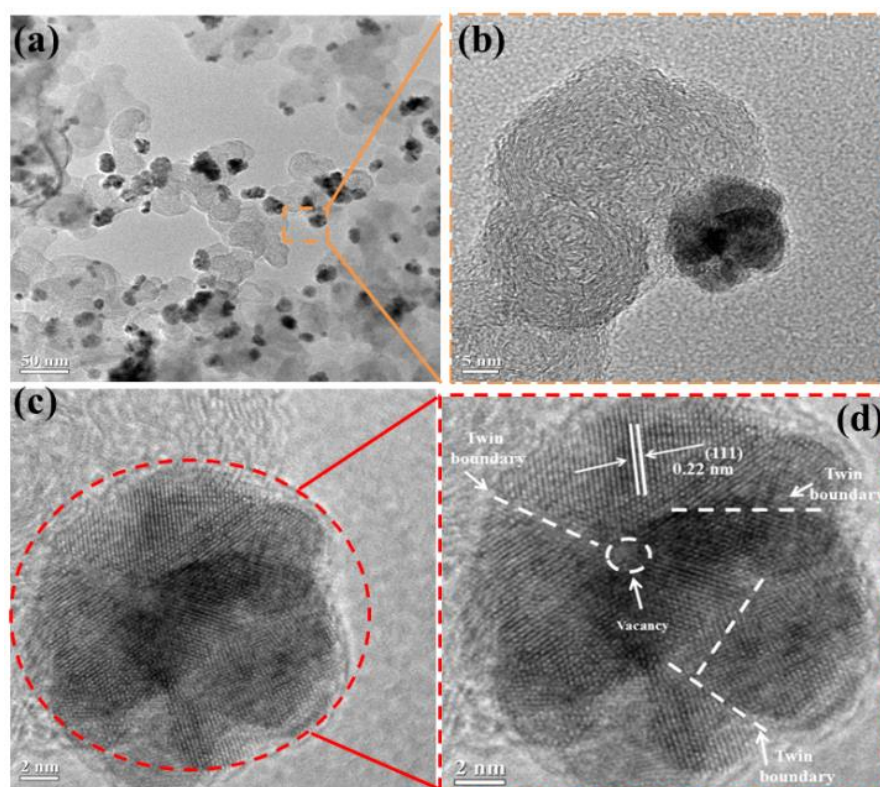

Figure 4B.5: TEM (a) and HRTEM (b-d) images of Pd_2CuCo/C NFs.

Elemental mapping analyses suggest homogeneous distribution of atoms on the surface of carbon, which further supports formation of alloy (Figure. 4B.6).
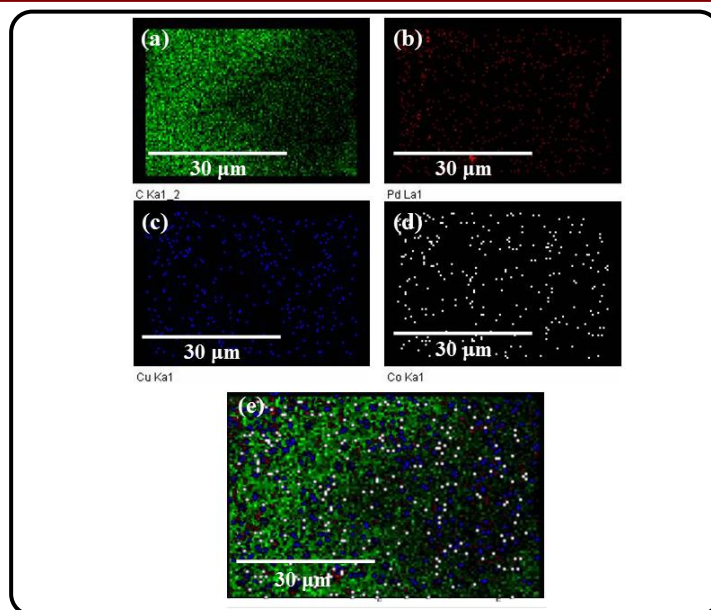
Figure 4B.6: EDS elemental mapping of (a) Carbon (b) Pd (c) Cu (d) Co and (e) overlap image of Pd$_2$CuCo/C NFs.

The NFs exhibit high specific surface area of 56.7 m^{2}g^{-1} and a large pore volume of 0.102 cc/g. The average pore diameter of 16.18 Å infers the mesoporous nature of NFs. The N$_2$ adsorption-desorption isotherm and corresponding pore size distribution of PCCC NFs are presented in Figure 4B.7.

Figure 4B.7: (a) N$_2$ adsorption-desorption isotherm of Pd$_2$CuCo/C NFs. (b) corresponding pore size distribution.
.

4B.1.2 Electrocatalytic Activity

The ECSAs of the catalysts were calculated from the CVs as presented in (Figure 4B.8). The measured ECSA of Pd_2CuCo NFs (100.94 m^2g^{-1}) wa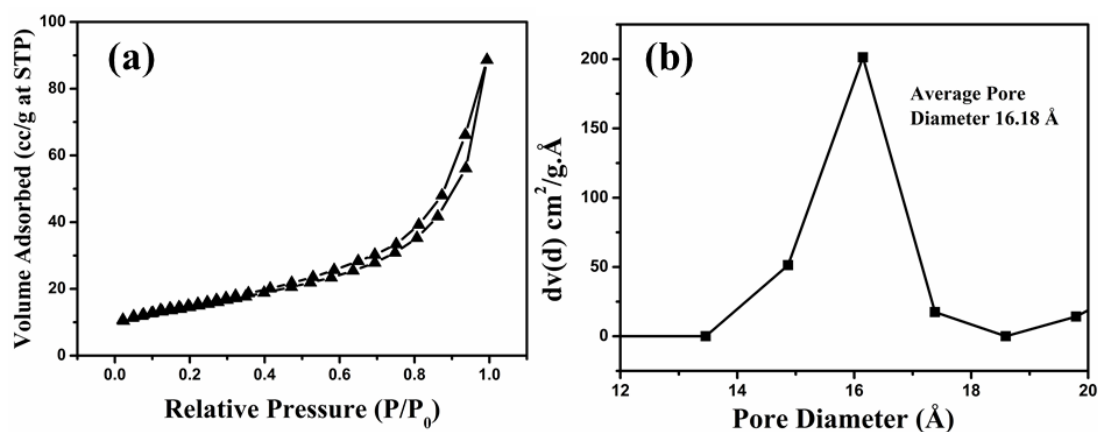s higher than that of the compared commercial Pt/C and Pd/C catalyst (8.7 m^2g^{-1} and 1.42 m^2g^{-1}, respectively).
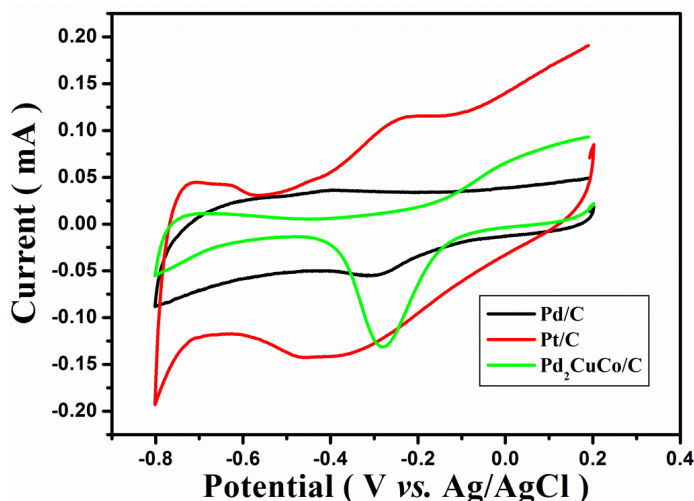

Figure 4B.8: CV plots of various NPs in the N_2-saturated 0.1 M KOH solution with a scan rate of 50 mV s^{-1}.

The electrocatalytic properties of PCCC NFs investigated in an aqueous solution of KOH (0.1 M). A strong peak at O_2-saturated KOH solution signifies that PCCC NFs has good ORR ability (Figure 4B.9a). For further understanding of the ORR kinetics, all the ECs are further examined by LSV in O_2-saturated 0.1M KOH at a rotating rate of 400, 900, 1600, 2500 and 3600 rpm as shown in Figure 4B.9b. By those polarization curves, the "n" transferred in the ORR process can be evaluated following K−L equation (details discussed in Chapter 3).

The K−L plots at a potential of −0.40, −0.50, −0.60, and −0.70 V show good linearity as shown in Figure 4B.9c, signifying that the ORR on PCCC NF follows first-order kinetics. From the slope (1/B) of the K−L plots, the "n" values for PCCC NFs at −0.40, −0.50, −0.60, and −0.70 V are calculated. Figure 4B.9d shows gives the corresponding "n" value *vs.* potential. It can be seen that the "n" values from −0.40 to −0.70 V are ~4.0, suggesting that the ORR mechanism on PCCC NF follows the direct "$4e-$" pathway ($O_2 + 2H_2O + 4e^- \rightarrow 4OH^-$).
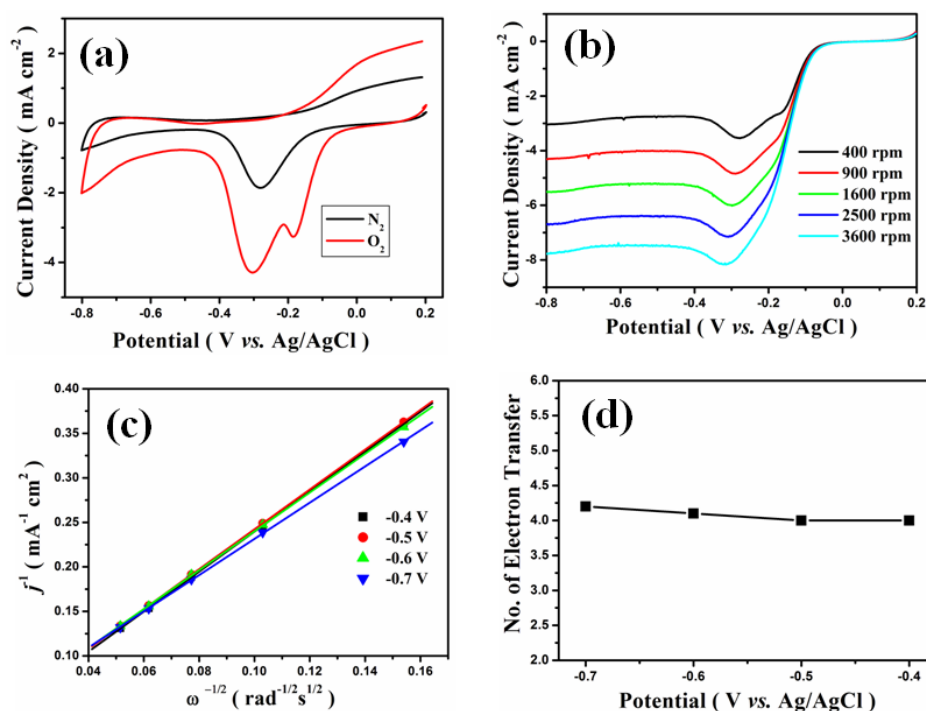
Figure 4B.9: (a) CV plots of Pd_2CuCo/C NFs, N_2- and O_2-saturated 0.1 M KOH solution with a scan rate of 50 mV s^{-1}, (b) Rotating rate-dependent ORR polarization curves for respective NC with the scan rate of 10 mV s−1, (c) K-L plots of j^{-1} vs. $\omega^{-1/2}$ for Pd_2CuCo/C NFs at different potential obtained from (b), and (d) The plot of the number of transferred electrons vs. potential for Pd_2CuCo/C NFs.

Figure 4B.10: (a) Comparison of rotating rate-dependent ORR polarization curves for different catalyst at 1600 rpm, (b) Tafel plots.

Figure 4B.10a shows the ORR polarization curves of various ECs (O_2-saturated 0.1 M KOH measured at 10 mV s^{-1}, and 1600 rpm at room temperature). The onset potential (E_{onset} = −0.018 V) and half-wave potential ($E_{1/2}$ = −0.138 V) of PCCC NF

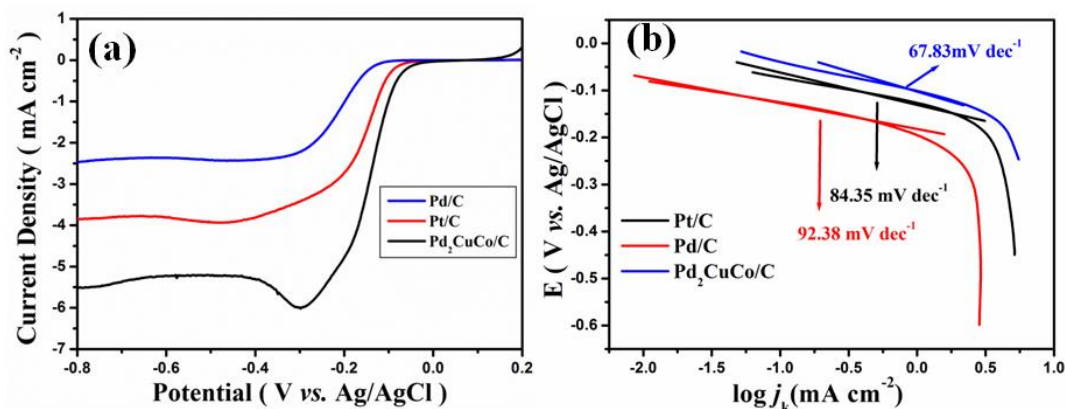EC are more positive than those of standard Pd/C ($E_{onset} = -0.103$ V, $E_{1/2} = -0.212$ V), Pt/C ($E_{onset} = -0.025$ V, $E_{1/2} = -0.154$ V), under the identical conditions, suggesting the superior ORR catalytic activity of ternary PCCC NF EC. Usually, the Tafel slope is used to assess the inherent catalytic activity of a catalyst towards ORR. The calculated Tafel slope PCCC NF (67.83 mV dec^{-1}) is lower than those of Pt/C (84.35 mV dec^{-1}) and Pd/C (92.38 mV dec^{-1}). This indicates that PCCC NF EC has improved kinetic behaviour and higher current density for ORR in comparison to other catalyst systems (Figure 4B.10b). The MA and SA for the different ECs, based on Figure 4B.10a, are presented in Figure. 4B.11. In general, the PCCC NF has the highest MA of 5300 mA mg^{-1}$_{Pd}$ among these three catalysts, which is 2.7 and 4.4 times larger than those for commercial Pt/C (1900 mA mg^{-1}$_{Pt}$) and Pd/C (1200 mA mg^{-1}$_{Pd}$) respectively and very interestingly about 12.04 times than that of the 2017 U.S. Department of Energy target (444 mA mg^{-1}$_{Pt}$) [4].

Figure 4B.11: (a) Mass activity and (b) Specific activity of ECs under different potential at 1600 rpm. (These values are calculated as per the loading mass of the Pd or Pt).

Moreover PCCC NFs had superior activity to the recently reported spherical PdCuCo (130 mA mg^{-1}$_{Pd}$) [31], anisotropic PdCuCo (180 mA mg^{-1}$_{Pd}$) [32] and Dendritic PdCuCo (380 mA mg^{-1}$_{Pd}$) [3]. The ORR SA of the PCCC NF reaches to 74.73 mA cm^{-2}, which is 1.38 and 2.20 times greater than the Pt/C and Pd/C, respectively.
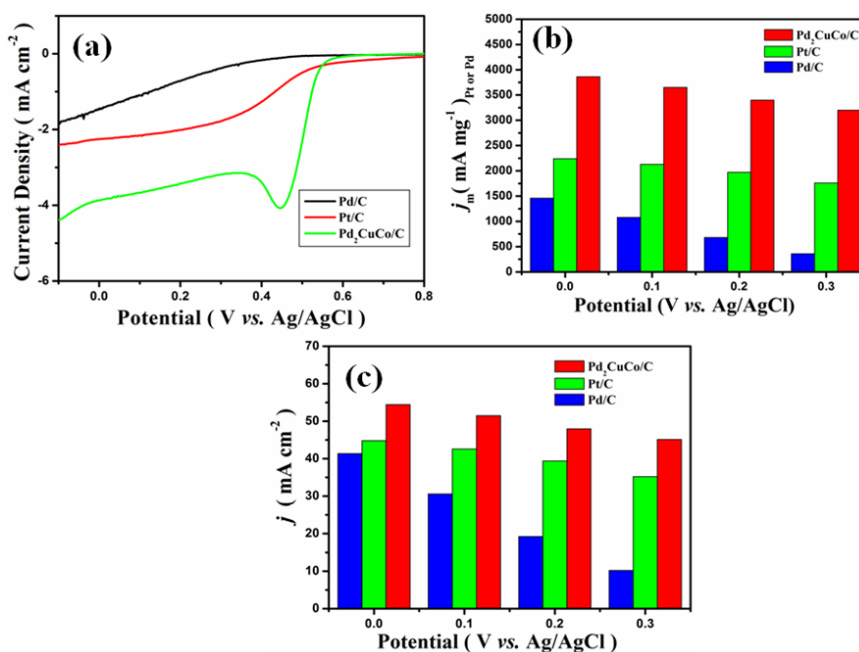
Figure 4B.12: (a) Comparison of rotating rate-dependent ORR polarization curves for different catalyst at 1600 rpm at 0.5 M $H_2SO_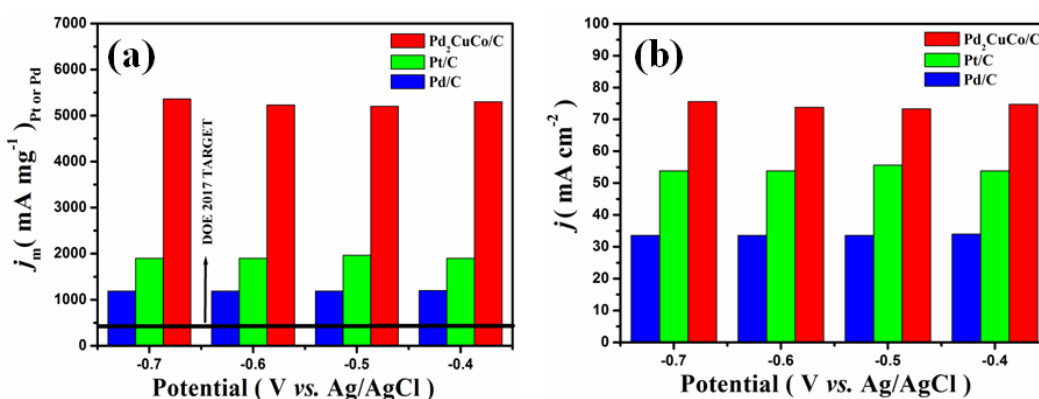4$ (b) Mass activities and (c) Specific activity of EC under different potential at 1600 rpm. (These values are calculated as per the loading mass of the Pd or Pt).
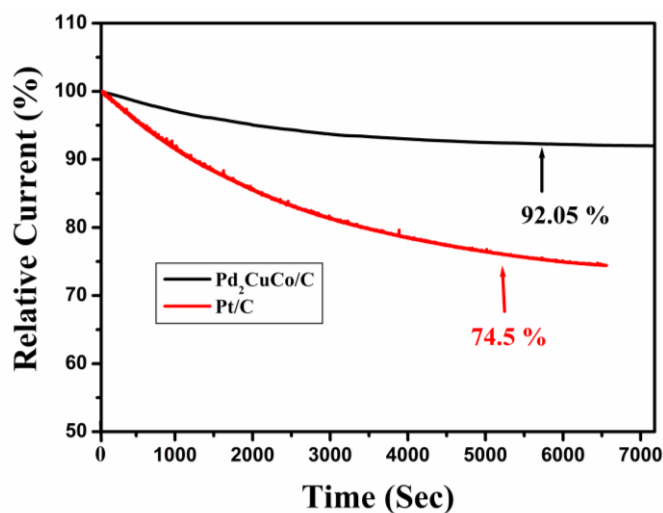
Figure 4B.13: CA curves of different catalysts, recorded at −0.3 V in O_2-saturated 0.1 M KOH solution with a rotation rate of 1600 rpm.

As shown in (Figure 4B.12), the electrocatalytic properties of PCCC NFs, the commercial Pd/C and Pt/C (20 wt %) were also evaluated in 0.5 M aqueous solution of H_2SO_4. The onset potential (E_{onset} = 0.597 V) and half-waved potential ($E_{1/2}$ = 0.50 V)

of PCCC NFs were positively shifted relative to standard Pd/C (E_{onset} = 0.292 V, $E_{1/2}$ = 0.38 V) and Pt/C (E_{onset} = 0.537 V, $E_{1/2}$ =0.41 V). The MA at 0.1 V of PCCC NFs (3650 mA mg^{-1}_{Pd}) was 1.71 and 3.37 fold higher than those of Pd/C (1080 mA mg^{-1}_{Pd}) and Pt/C (2130 mA mg^{-1}_{Pt}). The SA at 0.3 V of PCCC NFs (45.12 mA cm^{-2}) was 4.42-fold and 1.28-fold higher than those of Pd/C (10.19 mA cm^{-2}) and Pt/C (35.20 mA cm^{-2}), respectively. The electrochemical stability of PCCC NFs was evaluated by CA test as presented Figure 4B.13.

It can be observed that the initial activity decay for Pt/C is 25.5% after 6500 sec of testing, while the PCCC NFs catalyst shows only a loss of 7.95% of its initial activity, signifying the excellent stability of the PCCC NFs in alkaline media. To support this conclusion, an ADT was also performed for 1000 cycles between 0.2 V and −0.80V *vs*. Ag/AgCl at a scan rate of 100 mV s^{-1} in O_2-saturated 0.1 M KOH. The associated ORR polarization curves at 1600 rpm before and after 1000 CV cycles are presented in Figure.4B.14. The MA of PCCC NFs was declined to a lower extent (8.34%) in comparison to Pt/C (11%) after 1000 potential CV cycles. There is a clear drop of onset potential in case of Pt/C, whereas, the onset potential remains almost same after 1000 cycles for PCCC NFs catalyst. The $E_{1/2}$ of Pt/C (26 mV) also shows some definite change. But in case of PCCC NFs $E_{1/2}$ value remain same after 1000 cycles. The above discussion indicates that PCCC NFs is the most efficient catalyst for both alkaline and acidic media.
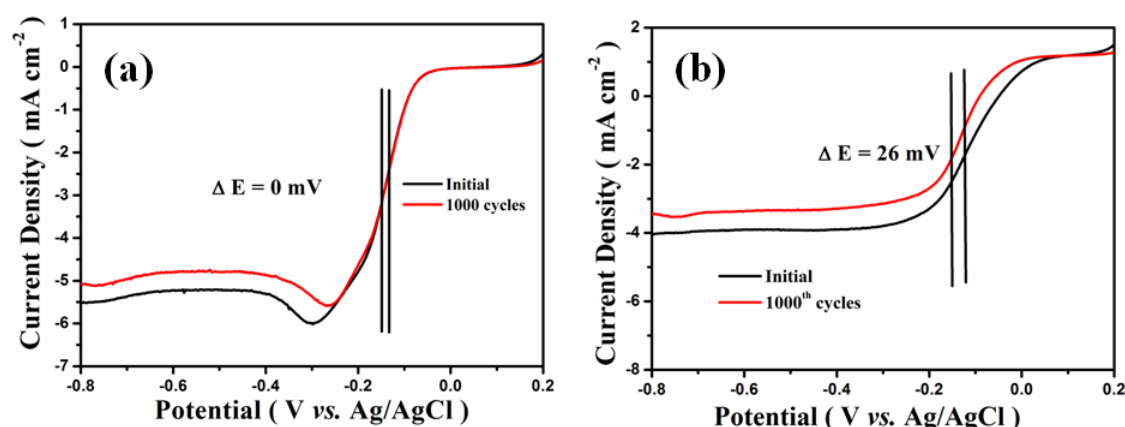

Figure 4B.14: (a) ORR polarization curves of Pd_2CuCo/C NFs and (b) ORR polarization curves of Pt/C at 1600 rpm before and after 1000 CV cycles.

The enhancement in the catalytic performance for ORR of the PCCC NF can be ascribed to the synergistic effect from the multiple structural and compositional advantages, such as (1) high surface area, due to the highly open structure and with porous morphology a large number of highly active and fully accessible catalytic sites, (2) exposed Pd (111) crystal planes, which is highly active plane for the ORR [33,34] (3) alloying with other transition metals, (Co, Cu, Fe, Ni, etc.) which effectively modified the electronic structure of Pd, thereby enhance the ORR activity of PCCC NF, (4) the half encapsulated structure of trimetallic NFs in carbon matrix empowers strong interaction among the two, inhibiting Pd_2CuCo NPs from detachment from the carbon matrix and amalgamation during the potential cycles. Since there is a stable electronic coupling between the carbon matrix and Pd_2CuCo NPs, this means the half embedded part possess very faster interfacial electron transfer ultimately enhancing the conductivity of PCCC NF. This leads to the acceleration of the ORR process. Moreover, surface defects are also believed to promote the catalytic activity by changing the surface electronic properties. In present case, NF possesses large number twinning defects accessible to the reactants is contributing to the enhancement of the catalytic activity by providing sufficient active sites.

Besides the structural and compositional advantages, the electronic property of the NF plays a vital rule in the superior ORR activity. The downshift of the d-band center promotes the improved performance of the Pd-based catalysts for ORR [35,36]. In practice, XPS measurement is used to characterize the d-band centers (εd, with respect to Fermi level). XPS spectra of Pd/C and PCCC are presented in (Figure 4B.4), the Pd $3d_{5/2}$ core-level binding energy of PCCC is found to be 336.02 eV, a positive shift of ~0.14 eV with respect to that of Pd/C (335.6 eV). This core-level B.E shift could be attributed to alloying Pd (fully occupied d-orbital) with Cu and Co (low occupancy d-orbital). In addition, due to the smaller lattice parameters of Cu and Co than Pd, the incorporation of Cu and Co into Pd would lead to the lattice contraction of Pd. The electron transfer effect and the shrunk lattice contribute a lowered d-band center of Pd, [37]. This would weaken the binding strength of reaction intermediates on the Pd surface, and then assist the electrocatalytic properties of the Pd based catalysts [38,39].

4B.2. Conclusions

This section of the chapter 4 presents a new strategy one-pot surfactant free synthesis of PCCC NFs with superior electrochemical performance for the ORR, The preferential exposure of (111) phase, multiple twin defects and lattice strain along with synergetic effects among the trimetallic alloy composition are the key factors for enhancement of electrocatalytic activity. The hierarchical PCCC NFs would have great potential in the real field of electrocatalysis because of the advantages of unique architectures, alloy composition of nanomaterial and simplistic synthetic procedure, which could provide a new approach for the development of practical catalysts in electrochemical fields.

References

[1] Zhou, W., Zhou, Z., Song, S., Li, W., Sun, G., Tsiakaras, P., and Xin, Q. Pt based anode catalysts for direct ethanol fuel cells. *Applied Catalysis B: Environmental*, 46(2):273−285, 2003.

[2] Ji, X., Lee, K. T., Holden, R., Zhang, L., Zhang, J., Botton, G. A., Couillard, M., and Nazar, L. F. Nanocrystalline intermetallics on mesoporous carbon for direct formic acid fuel cell anodes. *Nature Chemistry*, 2(4):286−293, 2010.

[3] Kim, Y., Noh, Y., Lim, E. J., Lee, S., Choi, S. M., and Kim, W. B. Star-shaped Pd@Pt core–shell catalysts supported on reduced graphene oxide with superior electrocatalytic performance. *J. Mater. Chem. A*, 2(19):6976−6986, 2014.

[4] Zhang, H., Jin, M., and Xia, Y. Enhancing the catalytic and electrocatalytic properties of Pt-based catalysts by forming bimetallic nanocrystals with Pd. *Chemical Society Reviews*, 41(24):8035−8049, 2012.

[5] Chen, A., and Ostrom, C. Palladium-based nanomaterials: synthesis and electrochemical applications. *Chemical Reviews*, 115(21):11999−12044, 2015.

[6] Fan, Z., Huang, X., Tan, C., and Zhang, H. Thin metal nanostructures: synthesis, properties and applications. *Chemical Science*, 6(1):95−111, 2015.

[7] Xiao, W., Liutheviciene Cordeiro, M. A., Gong, M., Han, L., Wang, J., Bian, C., Zhu, J., Xin, H. L., and Wang, D. Optimizing the ORR activity of Pd based nanocatalysts by tuning their strain and particle size. *Journal of Materials*

Chemistry A, 5(20):9867−9872, 2017.

[8] Lin, X.-X., Wang, A.-J., Fang, K.-M., Yuan, J., and Feng, J.-J. One-pot seedless aqueous synthesis of reduced graphene oxide (rGO)-supported core−shell Pt@Pd nanoflowers as advanced catalysts for oxygen reduction and hydrogen evolution. *ACS Sustainable Chemistry & Engineering*, 5(10):8675−8683, 2017.

[9] Chen, J., Lim, B., Lee, E. P., and Xia, Y. Shape-controlled synthesis of platinum nanocrystals for catalytic and electrocatalytic applications. *Nano Today*, 4(1):81−95, 2009.

[10] Bu, L., Tang, C., Shao, Q., Zhu, X., and Huang, X. Three-dimensional Pd$_3$Pb nanosheet assemblies: high-performance non-Pt electrocatalysts for bifunctional fuel cell reactions. *ACS Catalysis*, 8(5):4569−4575, 2018.

[11] Wang, H., Yin, S., Li, Y., Yu, H., Li, C., Deng, K., Xu, Y., Li, X., Xue, H., and Wang, L. One-step fabrication of tri-metallic PdCuAu nanothorn assemblies as an efficient catalyst for oxygen reduction reaction. *Journal of Materials Chemistry A*, 6(8):3642−3648, 2018.

[12] Shu, Y., Shi, X., Ji, Y., Wen, Y., Guo, X., Ying, Y., Wu, Y., and Yang, H. Hollow echinus-like PdCuCo alloy for superior efficient catalysis of ethanol. *ACS Applied Materials & Interfaces*, 10(5):4743−4749, 2018.

[13] Wang, X., Vara, M., Luo, M., Huang, H., Ruditskiy, A., Park, J., Bao, S., Liu, J., Howe, J., Chi, M., Xie, Z., and Xia, Y. Pd@Pt Core−shell concave decahedra: a class of catalysts for the oxygen reduction reaction with enhanced activity and durability. *Journal of the American Chemical Society*, 137(47):15036−15042, 2015.

[14] Wang, Y., Wang, W., Xue, F., Cheng, Y., Liu, K., Zhang, Q., Liu, M., and Xie, S. One-pot synthesis of Pd@Pt$_3$Ni core−shell nanobranches with ultrathin Pt$_3$Ni{111} skins for efficient ethanol electrooxidation.*Chemical Communications*, 54(41):5185−5188, 2018.

[15] Cui, X., Xiao, P., Wang, J., Zhou, M., Guo, W., Yang, Y., He, Y., Wang, Z., Yang, Y., Zhang, Y., and Lin, Z. Highly branched metal alloy networks with superior activities for the methanol oxidation reaction. *Angewandte Chemie International Edition*, 56(16):4488−4493, 2017.

[16] Jiang, Z., Jiang, Z.-J., Maiyalagan, T., and Manthiram, A. Cobalt oxide-coated

N- and B-doped graphene hollow spheres as bifunctional electrocatalysts for oxygen reduction and oxygen evolution reactions. *Journal of Materials Chemistry A*, 4(16):5877−5889, 2016.

[17] Xiong, Y., Xin, P., Chen, W., Wang, Y., Zhang, S., Ren, H., Rong, H., Zheng, X., Chen, C., Peng, Q., Wang, D., and Li, Y. PtAl truncated octahedron nanocrystals for improved formic acid electrooxidation. *Chemical Communications*, 54(32):3951−3954, 2018.

[18] Xia, Y., Hu, H., Shen, T., Bai, L., Xiang, S., Lei, Y., and Xiao, H. Hierarchically porous Pd nanospheres: facile synthesis and their application in HCOOH electrooxidation. *Chemical Communications*, 52(65):10064−10067, 2016.

[19] Liu, S., Zhang, Q., Li, Y., Han, M., Gu, L., Nan, C., Bao, J., and Dai, Z. Five-fold twinned Pd$_2$NiAg nanocrystals with increased surface Ni site availability to improve oxygen reduction activity. *Journal of the American Chemical Society*, 137(8):2820−2823, 2015.

[20] Liu, Y., Liu, S., Che, Z., Zhao, S., Sheng, X., Han, M., and Bao, J. Concave octahedral Pd@PdPt electrocatalysts integrating core–shell, alloy and concave structures for high-efficiency oxygen reduction and hydrogen evolution reactions. *Journal of Materials Chemistry A*, 4(42):16690−16697, 2016.

[21] Du, J., Chen, C., Cheng, F., and Chen, J. Rapid synthesis and efficient electrocatalytic oxygen reduction/evolution reaction of CoMn$_2$O$_4$ nanodots supported on graphene. *Inorganic Chemistry*, 54(11):5467−5474, 2015.

[22] Lu, Y., Zhao, S., Yang, R., Xu, D., Yang, J., Lin, Y., Shi, N.-E., Dai, Z., Bao, J., and Han, M. Well-coupled nanohybrids obtained by component-controlled synthesis and in situ integration of Mn$_x$Pd$_y$ nanocrystals on vulcan carbon for electrocatalytic oxygen reduction. *ACS Applied Materials & Interfaces*, 10(9):8155−8164, 2018.

[23] Chai, J., Li, F., Hu, Y., Zhang, Q., Han, D., and Niu, L. Hollow flower-like AuPd alloy nanoparticles: One step synthesis, self-assembly on ionic liquid-functionalized graphene, and electrooxidation of formic acid. *Journal of Materials Chemistry*, 21(44):17922−17929, 2011.

[24] Li, F., Li, J., Lin, X., Li, X., Fang, Y., Jiao, L., An, X., Fu, Y., Jin, J., and Li, R.

Designed synthesis of multi-walled carbon nanotubes@Cu@MoS$_2$ hybrid as advanced electrocatalyst for highly efficient hydrogen evolution reaction. *Journal of Power Sources*, 300:301−308, 2015.

[25] Parvez, K., Yang, S., Hernandez, Y., Winter, A., Turchanin, A., Feng, X., and Müllen, K. Nitrogen-doped graphene and its iron-based composite as efficient electrocatalysts for oxygen reduction reaction. *ACS Nano*, 6(11):9541−9550, 2012.

[26] Dehghani Sanij, F., and Gharibi, H. Preparation of bimetallic alloyed palladium-nickel electro-catalysts supported on carbon with superior catalytic performance towards oxygen reduction reaction. *Colloids and Surfaces A: Physicochemical and Engineering Aspects*, 538:429−442, 2018.

[27] Wu, Y., Cai, S., Wang, D., He, W., and Li, Y. Syntheses of water-soluble octahedral, truncated octahedral, and cubic Pt–Ni nanocrystals and their structure–activity study in model hydrogenation reactions. *Journal of the American Chemical Society*, 134(21):8975−8981, 2012.

[28] Zhao, L., Li, W., Zhou, J., Mu, X., and Fang, K. One-step synthesis of CuCo alloy/Mn$_2$O$_3$Al$_2$O$_3$ composites and their application in higher alcohol synthesis from syngas. *International Journal of Hydrogen Energy*, 42(27):17414−17424, 2017.

[29] Lian, C., Cheng, Y., Chen, L., Han, X., Lei, X., Liu, Y., and Wang, Y. Synthesis and electrocatalytic properties for oxygen reduction of Pd$_4$Fe nanoflowers. *Chemical Communications*, 54(51):7058−7061, 2018.

[30] Huang, L., Han, Y., and Dong, S. Highly-branched mesoporous Au-Pd-Pt trimetallic nanoflowers blooming on reduced graphene oxide as an oxygen reduction electrocatalyst. *Chemical Communications*, 52(56):8659−8662, 2016.

[31] Jiang, K., Wang, P., Guo, S., Zhang, X., Shen, X., Lu, G., Su, D., and Huang, X. Ordered PdCu-based nanoparticles as bifunctional oxygen-reduction and ethanol-oxidation electrocatalysts. *Angewandte Chemie International Edition*, 55(31):9030−9035, 2016.

[32] Zuo, Y., Rao, D., Li, S., Li, T., Zhu, G., Chen, S., Song, L., Chai, Y., and Han, H. Atomic vacancies control of Pd-based catalysts for enhanced electrochemical performance. *Advanced Materials*, 30(1):1704171, 2018.

[33] Ou, L., and Chen, S. Comparative study of oxygen reduction reaction mechanisms on the Pd (111) and Pt (111) surfaces in acid medium by DFT. *The Journal of Physical Chemistry C*, 117(3):1342−1349, 2013.

[34] Brandt, K., Steinhausen, M., and Wandelt, K. Catalytic and electro-catalytic oxidation of formic acid on the pure and Cu-modified Pd (111)-surface. *Journal of Electroanalytical Chemistry*, 616(1-2):27−37, 2008.

[35] Xue, H., Tang, J., Gong, H., Guo, H., Fan, X., Wang, T., He, J., and Yamauchi, Y. Fabrication of PdCo bimetallic nanoparticles anchored on three-dimensional ordered N-doped porous carbon as an efficient catalyst for oxygen reduction reaction. *ACS Applied Materials & Interfaces*, 8(32):20766−20771, 2016.

[36] Liu, D., Guo, Q., Hou, H., Niwa, O., and You, T. Pd_xCo_y nanoparticle/carbon nanofiber composites with enhanced electrocatalytic properties. *ACS Catalysis*, 4(6):1825−1829, 2014.

[37] Wang, L., Zhai, J.-J., Jiang, K., Wang, J.-Q., and Cai, W.-B. Pd–Cu/C electrocatalysts synthesized by one-pot polyol reduction toward formic acid oxidation: Structural characterization and electrocatalytic performance. *International Journal of Hydrogen Energy*, 40(4):1726−1734, 2015.

[38] Luo, L., Zhu, F., Tian, R., Li, L., Shen, S., Yan, X., and Zhang, J. Composition-Graded $Pd_xNi_{1−x}$ Nanospheres with Pt monolayer shells as high-performance electrocatalysts for oxygen reduction reaction. *ACS Catalysis*, 7(8):5420−5430, 2017.

[39] Hammer, B., and Nørskov, J. K. Theoretical surface science and catalysis—calculations and concepts. *Advances in Catalysis*. 45:71−129, 2000.